https://doi.org/10.5194/wes-2026-82
Preprint. Discussion started: 8 May 2026

eawe european academy of wind energy
Open Access WIND ENERGY SCIENCE DISCUSSIONS

Observations of wind ramps generated by thunderstorm outflows

Aliza Abraham[1], Nicola Bodini[1], Nicholas Hamilton[1], Brian Hirth[2], John Schroeder[2], and Patrick Moriarty[1]

[1]National Laboratory of the Rockies, Golden, CO, USA
[2]Texas Tech University, Lubbock, TX, USA

Correspondence: Aliza Abraham (aliza.abraham@nlr.gov)

Abstract. Thunderstorms occur frequently in regions with strong wind resources, such as the U.S. Great Plains. The outflows from these storms generate wind ramps, where the wind speed and direction change dramatically over a short period. Wind turbines are designed to withstand wind ramps such as the “extreme coherent gust with direction change" (ECD) defined by the International Electrotechnical Commission (IEC), but this depiction is highly simplified and based on point measurements. In the current investigation, we characterize the wind ramps generated by six thunderstorm outflows observed in northern Oklahoma using dual-Doppler X-band radar measurements covering a 160 km^3 volume, and compare their properties with the IEC-defined ECD. We show that, while the observed wind ramps exhibit wind speed and direction changes with similar magnitudes to the ECD, the observed rise times are an order of magnitude longer. Furthermore, the observed events are more complex than the idealized ECD profile, displaying spatial and temporal variations that cause significant variability in wind turbine power generation.

1 Introduction

Thunderstorms are common occurrences in the U.S. Great Plains region, with more than 15 severe thunderstorm watches recorded in counties in Iowa, Kansas, Oklahoma, and Texas in 2024 (Storm Prediction Center (SPC), NOAA, 2025). These four states also had the largest installed wind energy capacity in the same year, accounting for half of the wind energy capacity in the United States (U.S. Department of Energy, 2025). Thunderstorm outflows generate large changes in wind speed and direction over a short period of time, which can pose significant challenges to reliable wind power generation, both in terms of energy forecasting (Valldecabres et al., 2020) and structural loading (Kelly et al., 2021). Because of the overlap between thunderstorm activity and wind energy installations, thorough understanding of these thunderstorm outflow events and their impact on wind farms is needed to ensure the continued contribution of wind energy to the reliable operation of the electricity grid.

https://doi.org/10.5194/wes-2026-82
Preprint. Discussion started: 8 May 2026

eawe european academy of wind energy
Open Access WIND ENERGY SCIENCE DISCUSSIONS

Thunderstorm outflows, or gust fronts, are generated by the air diverging from the evaporatively cooled downdraft at the base of a storm (Wallace and Hobbs, 2006). These fronts propagate as density currents, driven by the pressure gradient induced by the cold air with high hydrostatic pressure (Wakimoto, 1982). Their properties were first characterized using Doppler radar in the 1980s, revealing their three-dimensional structure and the spatial variability of their shape and kinematics (Mahoney III, 1988). Since then, radar technology has evolved to capture these events in more detail, with dual-Doppler Ka-band radars used to measure wind ramps generated by thunderstorm outflows (Gunter and Schroeder, 2015) and cold fronts (Hirth et al., 2016). Profiling lidars have also been used to observe the properties of the vertical profiles of wind speed, direction, and turbulence during thunderstorm events (Canepa et al., 2020).

Several studies have investigated the ability of different models to capture strong wind ramp events, such as those generated by thunderstorm outflows. Valldecabres et al. (2020) showed that numerical weather prediction models fail to capture the magnitude and timing of wind ramp events, but the use of remote sensing data significantly improves short-term wind ramp forecasts. Similarly, the ability of the Weather Research and Forecasting model to capture the magnitude and timing of the cold front event described in Hirth et al. (2016) was significantly improved when nudging was used to match the outer domains to the observations (Arthur et al., 2020). Kelly et al. (2021) modeled the impact of ramps on wind turbine loads using large-eddy simulations based on an ensemble of wind velocity measurements taken over 11 years. Highlighting the spatial variability of a thunderstorm outflow using the measurements from multiple lidars, Pichugina et al. (2024) showed that the High-Resolution Rapid Refresh numerical weather prediction model also struggled to capture the timing and magnitude of the observed wind speed and direction changes. These studies emphasize the importance of observations to improve the understanding of and ability to predict thunderstorm outflows and other wind ramp events.

Recently, increased focus has been placed on evaluating wind ramp events in terms of their impact on wind turbines. This work has been conducted in reference to the International Electrotechnical Commission's (IEC) definition of an "Extreme coherent gust with direction change (ECD)" (IEC, 2019). Hannesdóttir and Kelly (2019) used meteorological mast data from three different wind energy test sites to develop a new method for characterizing wind ramps from wind speed and direction time series. They observed gusts with wind speed amplitudes comparable to those described in the IEC standard but with longer rise times and larger wind direction changes. Kelly et al. (2021) did not characterize wind direction changes, but they also reported much longer wind speed ramp rise times than those described in the standard (hundreds of seconds rather than 10 s).

In the current study, we aim to further assess the ability of the IEC standard to represent the events experienced by operational wind farms, focusing particularly on thunderstorm outflows. We fully characterize six thunderstorm outflow events, capitalizing on the extensive array of in situ and remote sensing instrumentation deployed for the AWAKEN campaign conducted over 2 years in the U.S. Great Plains region. In particular, the dual-Doppler X-band radar system measures the evolution of the outflows over a 30 km range, while lidars and turbine instrumentation capture their passage at high temporal resolution. We compare these detailed observations of thunderstorm outflows with the IEC ECD depiction to determine the accuracy of the simplified description of such complex events. Section 2 provides additional details about the relevant IEC standard, while Sect. 3 describes the AWAKEN campaign and the instruments used in the current investigation. Section 4 explains how thun-

https://doi.org/10.5194/wes-2026-82
Preprint. Discussion started: 8 May 2026

eawe european academy of wind energy
Open Access WIND ENERGY SCIENCE DISCUSSIONS

derstorm outflow events are identified, Sect. 5 describes the method used to automatically detect the outflow boundaries in the radar data, and Sect. 6 presents the wind ramp characterization process. The results of this characterization, along with a comparison with the IEC standard and a discussion of the implications for wind energy are presented in Sect. 7. Finally, Sect. 8 summarizes the key findings and proposes ideas for future work.

2 IEC standard for extreme coherent gust with direction change

The IEC specifies design requirements for wind turbines, including descriptions of conditions that they must be able to safely withstand. Wind ramps generated by thunderstorm outflows are best represented by the "extreme coherent gust with direction change (ECD)" (IEC, 2019). The ECD prescribes a wind speed change of $\Delta u = 15$ m s^{-1} and a rise time of $\Delta t = 10$ s. The wind speed changes over time as:

$$u(z,t) = \begin{cases} u_0(z) & \text{for } t \leq 0 \\ u_0(z) + 0.5\Delta u(1 - \cos(\pi t/\Delta t)) & \text{for } 0 \leq t \leq \Delta t \\ u_0(z) + \Delta u & \text{for } t \geq \Delta t \end{cases}. \tag{1}$$

Here, z is the height above ground, t is the time elapsed, and $u_0(z)$ is the initial wind speed profile as defined by the power law, with $\alpha = 0.2$:

$$u_0(z) = u_{\text{hub}}(z/z_{\text{hub}})^{\alpha}. \tag{2}$$

The hub height and initial hub-height wind speed are represented by z_{hub} and $u_{0,\text{hub}}$, respectively. The wind direction change magnitude depends on $u_{0,\text{hub}}$ as:

$$\Delta\theta = \begin{cases} 180^\circ & \text{for } u_{0,\text{hub}} < 4 \text{ m s}^{-1} \\ \frac{720^\circ (\text{m s}^{-1})}{u_{0,\text{hub}}} & \text{for } 4 \text{ m s}^{-1} < u_{0,\text{hub}} \end{cases}. \tag{3}$$

The wind direction change over time is then defined as:

$$\theta(t) = \begin{cases} 0 & \text{for } t \leq 0 \\ \pm 0.5\Delta\theta(1 - \cos(\pi t/\Delta t)) & \text{for } 0 \leq t \leq \Delta t \\ \pm\Delta\theta & \text{for } t \geq \Delta t \end{cases}, \tag{4}$$

with a constant value of θ with height. Note that the variable names have been changed from those used in IEC (2019) for consistency with the rest of the current manuscript. Example ECD wind speed and wind direction time series are shown in Fig. 1 for $u_{0,\text{hub}} = 11$ m s^{-1}, with Δu, $\Delta\theta$, and Δt labeled on the plots.

https://doi.org/10.5194/wes-2026-82
Preprint. Discussion started: 8 May 2026

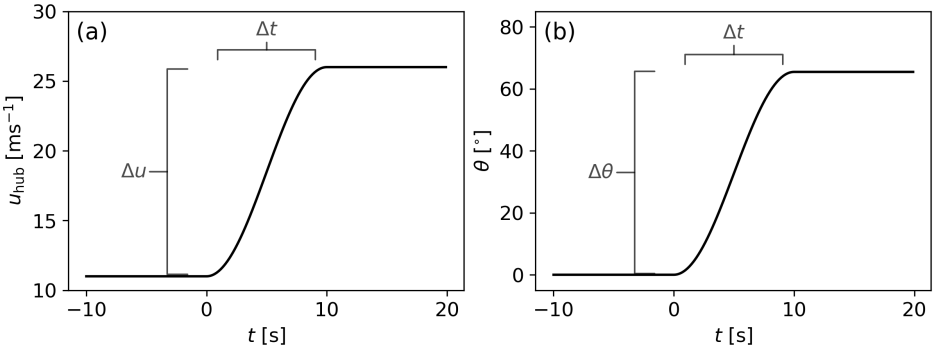

Figure 1. Time series for (a) hub-height wind speed and (b) wind direction following the IEC standard for an "extreme coherent gust with direction change (ECD)" with $u_{0,\mathrm{hub}} = 11$ m s^{-1}. Key parameters, including Δu, $\Delta\theta$, and Δt, are labeled on the plots.

3 AWAKEN campaign

The American WAKE ExperimeNt (AWAKEN) was a multi-year, multi-institutional campaign conducted in northern Oklahoma, designed to advance the understanding of interactions between wind farms and the atmosphere (Moriarty et al., 2024). The AWAKEN site (Fig. 2) encompassed a region of relatively simple terrain, land cover of agricultural crops and grassland, and multiple operational wind farms. The site was heavily instrumented with in situ and remote sensing devices for measuring wind, temperature, and precipitation. The instruments used in the current investigation are discussed in more detail below.

3.1 Dual-Doppler X-band radars

The primary instrument used for the following analysis is the dual-Doppler X-band radar system (Hirth et al., 2024). Two X-band radars were deployed at the locations marked "North radar" and "South radar" in Fig. 2. They each measured the along-beam (radial) wind speed in overlapping horizontal sectors of 145° at a resolution of 30°s^{-1}. They covered these sectors 18 times, at elevation angles between 0° and 1.7° for the south radar and between 0.1° and 1.8° for the north radar, completing the entire scan pattern in 124 s. The along-beam resolution of the radial wind speed is 9 m, and the across-beam resolution is 0.5° in both the horizontal and vertical directions (Hirth and Zalkind, 2025a, b).

Dual-Doppler reconstruction is used to obtain the horizontal wind speed magnitude and wind direction from the radial wind speeds measured by both radars. First, quality control removes erroneous velocity returns, then the radial wind speeds are interpolated onto a three-dimensional Cartesian grid spanning the region labeled "Radar domain" in Fig. 2. The grid has a horizontal resolution of 50 m and a vertical resolution of 25 m (10 levels between 375 m and 600 m above mean sea level, or MSL). The interpolated wind speed volumes from each radar are paired with the concurrent volume from the other radar; then, they undergo dual-Doppler reconstruction to convert the radial wind speed measurements from both radars into a volume of horizontal velocity vectors with wind speed magnitudes and directions (Hirth and Zalkind, 2025c). Because the two radars are not synchronized, the temporal resolution of the resulting vector volumes is between 2 and 4 minutes.

https://doi.org/10.5194/wes-2026-82
Preprint. Discussion started: 8 May 2026

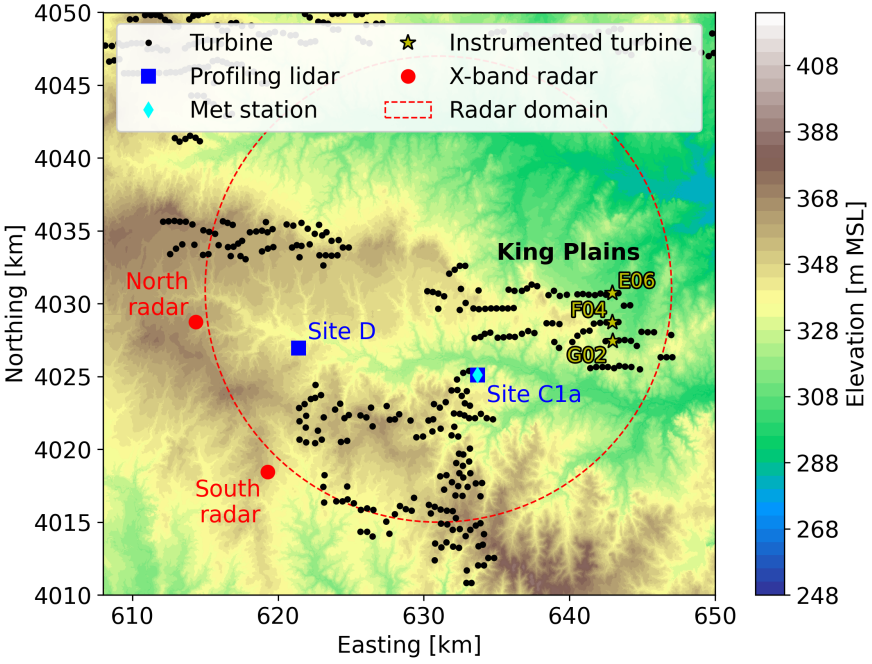

Figure 2. Map of the AWAKEN domain showing terrain elevation relative to mean sea level (MSL). Wind turbines, including the King Plains wind farm, are marked, along with the locations of key instruments.

3.2 Profiling lidars

Two profiling lidars are used in the current study. The first is a Vaisala Windcube v2, deployed at Site D (Fig. 2), which records wind speed and direction along a vertical profile at heights spanning 40 m to 200 m above ground level (AGL). The vertical resolution is 10 m up to 100 m, where it switches to 20 m until 200 m. With a terrain height of 343 m MSL at Site D, the vertical range corresponds to 383–543 m MSL. The lidar conducts a five-beam profiling scan, including one vertical beam, which takes ~ 5 s to complete. Wind speed and direction values are reconstructed from the five most recent beams every second. Data points with carrier-to-noise ratio values less than -23 dB are removed.

A Vaisala Windcube v1 is deployed at Site C1a (Fig. 2), measuring wind speed and direction between 40 m and 220 m AGL, or 368–548 m MSL (terrain height is 328 m MSL at Site C1a), at a constant vertical resolution of 20 m. The four-beam profiling scan (no vertical beam) produces independent horizontal wind speed and direction measurements every 4 s. A carrier-to-noise ratio threshold of -22 dB is applied to this dataset. These lidars are used because they capture wind measurements from the lower elevations around wind turbine rotor heights, highlighting the relevance of our findings for wind energy applications. They are also located close to the center of the radar domain, facilitating comparison between the instruments.

https://doi.org/10.5194/wes-2026-82
Preprint. Discussion started: 8 May 2026

eawe european academy of wind energy
Open Access WIND ENERGY SCIENCE DISCUSSIONS

3.3 Meteorological station

A surface meteorological (met) station is also deployed at Site C1a (Fig. 2) to supplement the remote sensing measurements with in situ data (Goldberger, 2024). The met station includes a RM Young 05106 Wind Monitor, which records the vector-averaged wind speed and direction over 1-minute intervals, installed 3 m above the ground. Vaisala temperature and humidity and barometric pressure sensors are also installed at 2 m and 1.6 m, respectively, recording at the same 1-minute frequency as the wind monitor. While many similar met stations are deployed throughout the AWAKEN domain, the station at Site C1a is used because of its situation near the center of the radar domain.

3.4 Turbine nacelle anemometers

Wind speeds measured by the cup anemometers located on the nacelles of the instrumented turbines highlighted in Fig. 2 are used to investigate the spatial variability of the thunderstorm outflow wind ramp events. Measurements are recorded every ~ 5 s by the turbine supervisory control and data acquisition system. Although all turbines record wind speed, turbines E06, F04, and G02 are selected due to their north–south alignment at the widest part of the King Plains wind farm, enabling comparisons between wind farm rows.

4 Event identification

Wind ramps are detected using the wind speed measured by the met station at Site C1a. Ten-minute averages of the 1-minute-resolution horizontal wind speed recorded by the met station are calculated, then occurrences where the wind speed changes at least 4 m s^{-1} between adjacent 10-minute periods are identified. An example of one such event from 2023-06-16 is presented in Fig. 3, with the detected period marked in red. Twenty-six of these wind ramp events are identified between December 2022 and July 2024. For each detected event, weather radar and dual-Doppler X-band radar data are manually inspected. If precipitation is observed in the weather radar and high-quality dual-Doppler radar data cover the entire domain, an event is selected for further analysis. Of the 26 events identified, six are analyzed in detail. Note that the selection of six events over 20 months is not intended to provide an assessment of the frequency of such events. For the current investigation, consistent dual-Doppler radar coverage is required to fully characterize the spatial and temporal evolution of the thunderstorm outflows observed; events without such coverage are excluded here.

5 Outflow boundary detection

For each event, the dual-Doppler radar dataset is manually inspected to determine the time period when the thunderstorm outflow boundary is within the radar volume. In each case, the boundary is clearly visible as a sharp change in both the wind speed and direction fields from the radars, as seen in Fig. 4(a) and (b), respectively. The following procedure is used to automatically detect the boundary in the radar data with the scikit-image Python package (van der Walt et al., 2014): At each time stamp and at each height, histograms of wind speed and direction are generated. These histograms exhibit bimodal distributions, repre-

https://doi.org/10.5194/wes-2026-82
Preprint. Discussion started: 8 May 2026

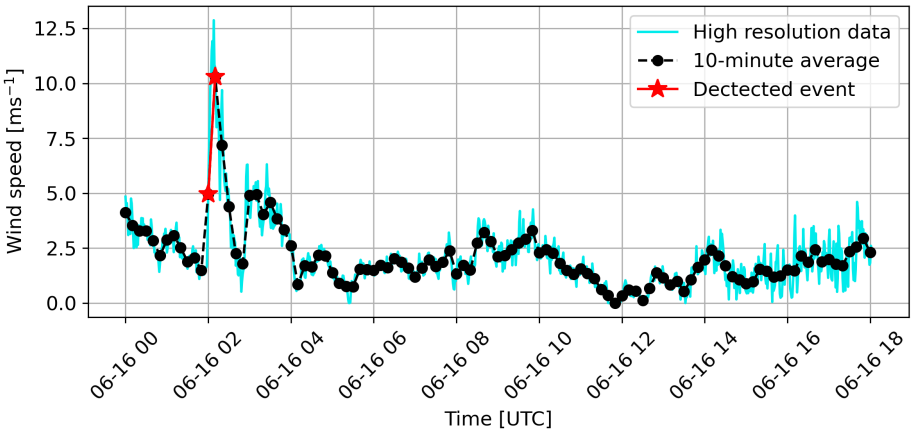

Figure 3. Time series of high-resolution (1-minute) and 10-minute averaged wind speed recorded by the met station at Site C1a. A wind ramp with a wind speed change greater than 5 m s^{-1} is highlighted in red at ∼02 UTC.

senting the distinct regions upstream and downstream of the outflow boundary (Fig. 4(c) and (d)). To identify the boundary between these regions, hysteresis thresholds are applied to the wind speed and direction fields. Hysteresis thresholds maximize region connectivity by using two threshold values – regions above the low threshold are considered above the threshold if they are connected to regions above the high threshold. Here, the two threshold values are determined using the values of the low and high histogram peaks, $x_{p,\text{low}}$ and $x_{p,\text{high}}$, respectively:

$$\begin{aligned} x_{t,\text{low}} &= x_{p,\text{low}} + 0.3(x_{p,\text{high}} - x_{p,\text{low}}) \\ x_{t,\text{high}} &= x_{p,\text{high}} - 0.3(x_{p,\text{high}} - x_{p,\text{low}}) \end{aligned}, \tag{5}$$

where $x_{t,\text{low}}$ and $x_{t,\text{high}}$ are the low and high threshold values, respectively, shown as vertical dashed lines in Fig. 4(c) and (d). This thresholding process yields the binary images in Fig. 4(e) and (f). Next, Canny edge detection (Canny, 1986) is used to identify the edges between regions in the binary images. The largest edge with an eccentricity of at least 0.97 is selected as the outflow boundary, highlighted by the cyan and yellow lines in Fig. 4(e) and (f). Superimposing these lines back onto the radar fields shows that this method successfully identifies the locations of the boundaries between the distinct wind speed and direction regions (Fig. 4(g) and (h)).

From Fig. 4(g) and (h), it is clear that the identified edges for wind speed and direction are not coincident. This discrepancy between the wind speed and direction boundaries was observed in all six cases to varying extents. Figure 5 shows examples of both boundaries from three events, including the 2023-06-16 case discussed above. In the first case (2023-06-10), the boundary defined by the wind direction is smooth and slightly curved, while the wind speed boundary is jagged and irregular. In the 2023-06-16 case, the wind speed boundary is smoother and straighter than the wind direction boundary. The third case (2023-06-18) exhibits the most similar wind speed- and direction-defined boundaries, although some small deviations exist. Previous thunderstorm outflow studies have observed that wind speed and direction changes are not concurrent. Wakimoto (1982) found

https://doi.org/10.5194/wes-2026-82
Preprint. Discussion started: 8 May 2026

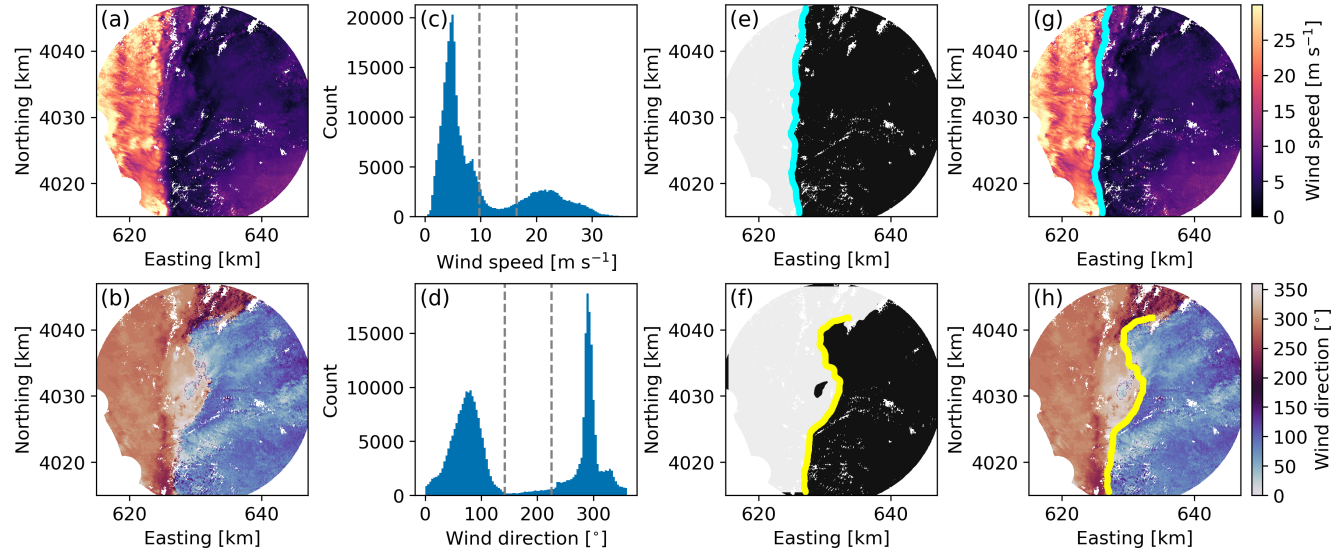

Figure 4. Automated outflow boundary detection procedure, starting with the wind speed (a) and direction (b) fields from the dual-Doppler X-band radar system at one height (450 m MSL) and one time where the boundary is within the radar domain (2023-06-16 01:52:28 UTC), and the histograms generated from these fields (c and d). High and low hysteresis threshold values are indicated by vertical dashed gray lines. Binary images generated by thresholding the wind speed (e) and direction (f) fields, with the detected boundaries superimposed in cyan and yellow. (g and h) Radar images with the boundaries superimposed.

that the wind direction changed before the wind speed, consistent with all cases presented here where the wind direction boundary precedes the wind speed boundary, considering the outflows propagate (south)eastward. For the following analysis, we select the smoother of the two edges as the outflow boundary definition. In five of the six cases (the 2023-06-16 case is the exception), the boundary defined by the wind direction is smoother, so it is used to define the outflow boundary.

6 Wind ramp characterization

Once the coordinates of the thunderstorm outflow boundary have been defined for each of the six cases at each point in time and at each height, its properties can be characterized. The purpose of this characterization process is twofold: First, we aim to obtain the same parameters defined in Sect. 2 to facilitate comparison with the IEC standard. Second, we seek to gain additional physical insights into the behavior of thunderstorm outflows. With the dual-Doppler X-band radar data, we use the spatial variations in wind speed and direction to evaluate the properties of the outflow boundary rather than the temporal variations used in previous studies. This approach is selected because radar data have a spatial resolution of 50 m and a temporal resolution of 2 minutes. For a wind speed of 10 m s^{-1}, 50 m spatial resolution translates to 5 s temporal resolution, much finer than the native 2-minute temporal resolution. Therefore, we first quantify the propagation speed of the outflow boundary as a way to translate spatially defined quantities to temporal quantities, as defined in the IEC standard. Note that

https://doi.org/10.5194/wes-2026-82
Preprint. Discussion started: 8 May 2026

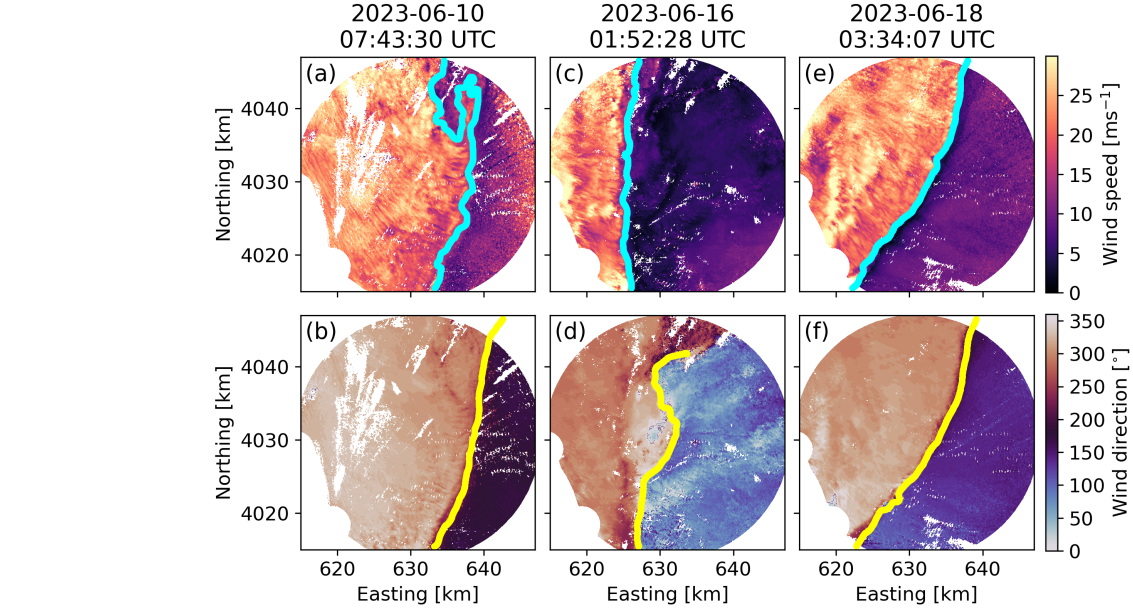

Figure 5. Examples of wind speed (top row) and direction (bottom row) fields from the dual-Doppler X-band radar data at 450 m MSL for three thunderstorm outflow cases, with automatically detected boundaries superimposed in cyan and yellow. Each column is labeled with the time stamp for the case shown.

a comparison between the spatially defined characterization from the radar and temporally defined characterization from two lidars is presented in Sect. 6.3.

6.1 Propagation speed

To compute the propagation speed of the outflow boundary, we first calculate the displacement of the boundary between adjacent time steps. Because of the circular shape of the radar domain, the length of the front within the domain changes over time. Therefore, we select the shortest of the two boundaries between adjacent time steps; then, for each point along the boundary in the selected time step, we find the nearest boundary point in the neighboring time step. The distance between each point and its nearest neighbor in the adjacent time step is recorded, and the mean of all the distances along the boundary is computed. This mean is considered the propagation distance of the front between the two time steps. The elapsed time is then used to calculate the propagation speed within that interval.

No substantial variation in propagation speed with height is observed within the elevation range of the radar volume, so the median values for each case at each time from when the boundary enters the radar domain are presented in Fig. 6. All measured outflow boundaries propagate between $\sim$10 and 20 m s^{-1}, with low levels of acceleration or deceleration. The 2023-07-01 boundary experiences the largest acceleration at an overall rate of 0.003 m s^{-2}, and the 2024-05-24 exhibits the largest deceleration at -0.004 m s^{-2}.

https://doi.org/10.5194/wes-2026-82
Preprint. Discussion started: 8 May 2026

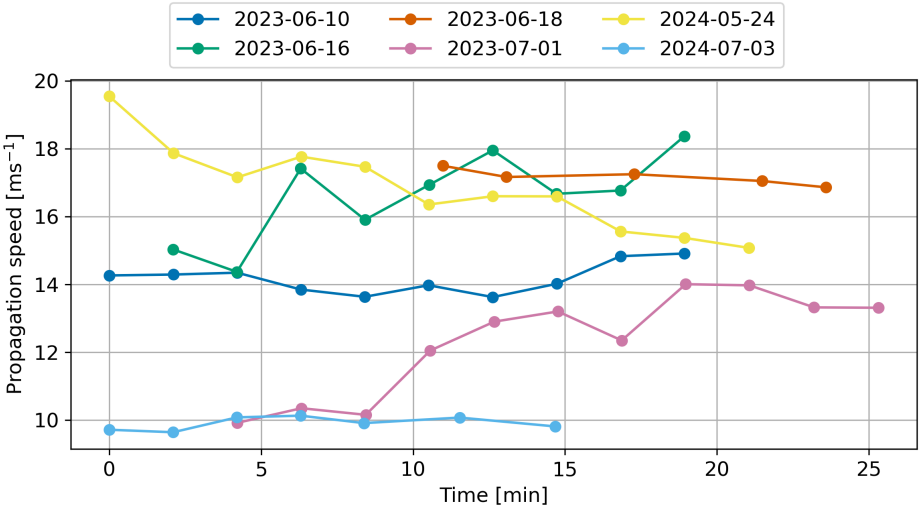

Figure 6. Propagation speed of each thunderstorm outflow event over time, calculated as the median over heights [375, 450, 525, 600] m MSL. Time is measured from when the outflow boundary enters the radar domain.

Previous studies have discussed the applicability of the density current model to thunderstorm outflows, showing that they follow the expected relationship between propagation speed and pressure change across the outflow boundary (Wakimoto, 1982; Droegemeier and Wilhelmson, 1987; Mahoney III, 1988). The theoretical propagation speed can be calculated as:

$$V = k(\Delta P/\rho)^{1/2}, \tag{6}$$

where ΔP is the pressure change across the outflow boundary, ρ is the density of surrounding air, and k is a constant, the internal Froude number. These atmospheric data are taken from the met station at Site C1a (Sect. 3.3), with ρ defined as the mean density in the hour before the outflow, and ΔP defined as the difference between the maximum pressure after the outflow passes and the mean pressure in the hour before. The temporal mean of the propagation speed plotted in Fig. 6 is then used to compute k for each case, except the 2023-06-18 case, for which the atmospheric data are unavailable. The values of k for the other five cases range between 0.71 and 1.21, in good agreement with values reported in previous studies (Wakimoto, 1982; Droegemeier and Wilhelmson, 1987; Mahoney III, 1988).

6.2 Ramp function fit

To characterize the wind speed and direction changes (wind ramp) across the outflow boundary, we adapt the methodology developed by Hannesdóttir and Kelly (2019) to the spatially varying flow fields studied here. At each time when the outflow boundary is within the radar domain and at each height, the line perpendicular to each point along the boundary is identified (Fig. 7(a)). The cross sections of wind speed and direction from the radar data along this line are extracted and normalized using their mean and standard deviations, then a continuous wavelet transform is performed on each using the first derivative

https://doi.org/10.5194/wes-2026-82
Preprint. Discussion started: 8 May 2026

eawe european academy of wind energy
Open Access WIND ENERGY SCIENCE DISCUSSIONS

Table 1. Outflow boundary propagation speeds (V), pressure changes (ΔP), and air densities (ρ) used to calculate the Froude number (k) for each case. "N/A" indicates data are not available.

Case	V [m s^{-1}]	ΔP [kPa]	ρ [kg m^{-3}]	k
2023-06-10	14.2	0.366	1.13	0.79
2023-06-16	16.6	0.610	1.12	0.71
2023-06-18	17.2	N/A	N/A	N/A
2023-07-01	12.3	0.115	1.11	1.21
2024-05-24	16.8	0.346	1.13	0.96
2024-07-03	9.9	0.208	1.09	0.72

of a Gaussian wavelet. The peak of the wavelet transform localizes the wind ramp along the perpendicular line and identifies its length scale (Fig. 7(b) and (c)).

Next, idealized ramp functions are fit to the cross sections of wind speed and direction along the perpendicular line. The ramp functions are based on the error function:

$$\begin{aligned} u(d) &= \frac{u_{\text{up}}+u_{\text{down}}}{2} + \frac{u_{\text{up}}-u_{\text{down}}}{2}\text{erf}\left(\frac{d-d'_u}{\delta_u}\right) \\ \theta(d) &= \frac{\theta_{\text{up}}+\theta_{\text{down}}}{2} + \frac{\theta_{\text{up}}-\theta_{\text{down}}}{2}\text{erf}\left(\frac{d-d'_\theta}{\delta_\theta}\right) \end{aligned}, \tag{7}$$

where u_{up} and u_{down} are the wind speeds upstream and downstream of the boundary, and θ_{up} and θ_{down} are the upstream and downstream wind directions. The distance from the boundary is d, and d'_u and d'_θ indicate the location of the wind speed and direction ramps, respectively, obtained from the wavelet transform. The constants δ_u and δ_θ are used to calculate the wind speed and direction rise distance, explained in more detail below.

The unknown parameters (u_{up}, u_{down}, and δ_u for wind speed and θ_{up}, θ_{down}, and δ_θ for wind direction) are obtained by fitting the idealized ramp function to a section of the wind speed and direction cross sections. The length of the section is 3 times the length scale obtained from the wavelet transform, centered on d'_u and d'_θ, trimmed to remain within the boundaries of the radar domain. The result of the curve-fitting procedure is used to calculate wind speed and direction amplitudes (Δu and $\Delta\theta$) and rise distances (Δd_u and Δd_θ), as follows:

$$\begin{aligned} \Delta u &= u_{\text{up}} - u_{\text{down}} \\ \Delta d_u &= 3.17\delta_u \\ \Delta\theta &= \theta_{\text{up}} - \theta_{\text{down}} \\ \Delta d_\theta &= 3.17\delta_\theta \end{aligned}. \tag{8}$$

Multiplying δ by 3.17 gives the distance over which the wind speed or direction rises from 1% to 99% of its final values. The above procedure is shown in Fig. 7, and the final parameters are labeled on panels (d) and (e).

One additional step is required to compare the parameters obtained from the radar data with those defined by the IEC, presented in Sect. 2. The IEC uses rise time (Δt) rather than rise distance, as most wind speed measurements for wind energy applications are collected using point measurements such as anemometers. We divide Δd_u and Δd_θ by the boundary propa-

https://doi.org/10.5194/wes-2026-82
Preprint. Discussion started: 8 May 2026

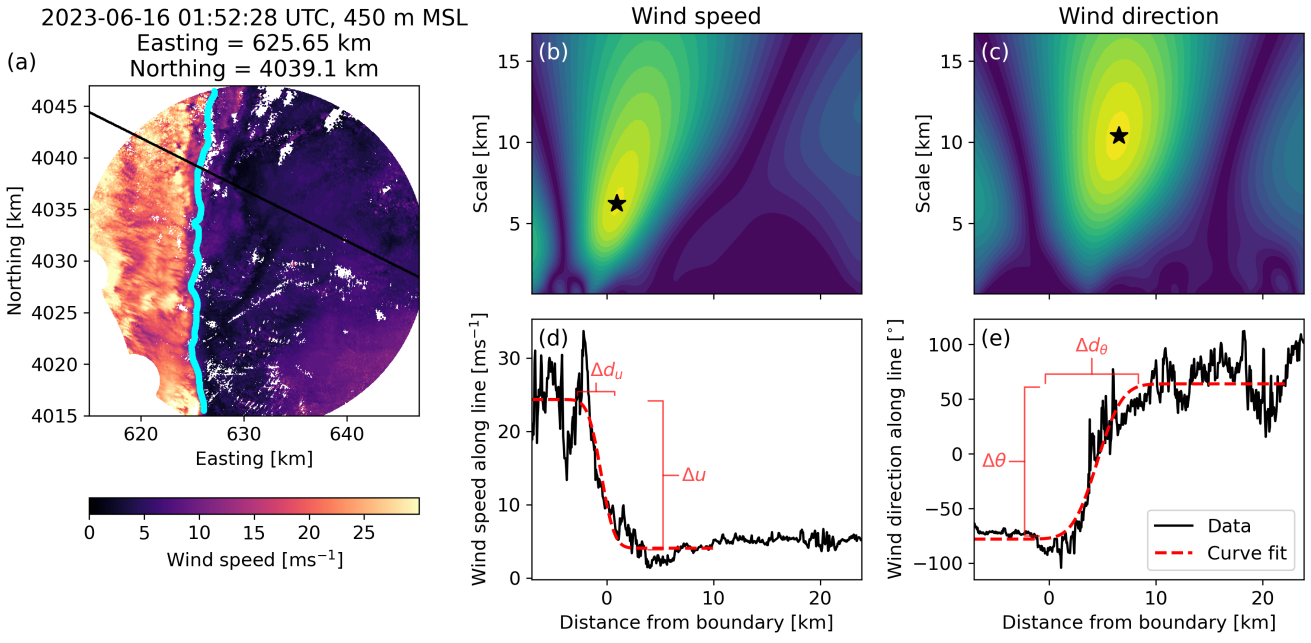

Figure 7. Example of the wind ramp characterization procedure showing (a) the wind speed field from the radar data, along with the outflow boundary in cyan and the line perpendicular to one point on the boundary in black. Continuous wavelet transforms of the wind speed (b) and direction (c) cross sections along the black line in (a). The black stars mark the peaks of the transforms. Wind speed (d) and direction (e) cross sections, along with the curve fit. The parameters obtained from the curve fit are labeled in red.

gation speed to get the rise times, Δt_u and Δt_θ. It must also be noted that the IEC uses the same value of Δt for the wind speed and direction rise time, while we have defined two different values for the two quantities. As observed in Sect. 5, the wind speed and direction do not change at exactly the same time or location in space. Therefore, we do not expect them to necessarily change at the same rate. Indeed, in the example shown in Fig. 7, the wind direction changes much more gradually than the wind speed.

6.3 Comparison of spatial and temporal definitions

To determine the validity of the transformation from the spatially varying to temporally varying perspective, we apply the ramp-fitting procedure to high-temporal-resolution data collected by two lidars within the radar domain at Site D and Site C1a (see Fig. 2). We then compare the results obtained from the lidars with those obtained from the spatially varying radar data at the same locations. Figure 8 presents this comparison for the 2023-06-16 case at Site D, which the outflow boundary crosses at 01:48:16 UTC. Panels (b) and (c) show the wind speed and direction cross sections from the radar data along the line intersecting Site D at a height of 450 m MSL, with the ramp function fit superimposed. Panels (d) and (e) show the time series of wind speed and direction at Site D from the lidar (blue) and radar (gray), along with the ramp function fit to the lidar data. From

https://doi.org/10.5194/wes-2026-82
Preprint. Discussion started: 8 May 2026

these panels, it is clear that both instruments capture the large-scale temporal variations well, but the temporal resolution of the radar is too low to be used to characterize the wind ramp. The low temporal resolution of the radar is the reason the spatially varying data are used to characterize the wind ramps instead of the temporally varying data from the radar, as discussed in the first paragraph of Sect. 6. Note that the temporal resolution is relatively low because the radar scan was designed to span a large area – higher temporal resolution could be achieved with a targeted scan covering a narrower region. The lidar data are interpolated to the same height as the radar data, 107 m AGL, based on the terrain height at Site D (343 m MSL). The resulting ramp parameters from both the spatially varying radar data and temporally varying lidar data are presented in panels (f–i). To facilitate the comparison, the radar data are binned by their location along the boundary into 25 bins of ~ 1 km. The median of each bin is shown in black, with the shaded gray region indicating the interquartile range of the bins.

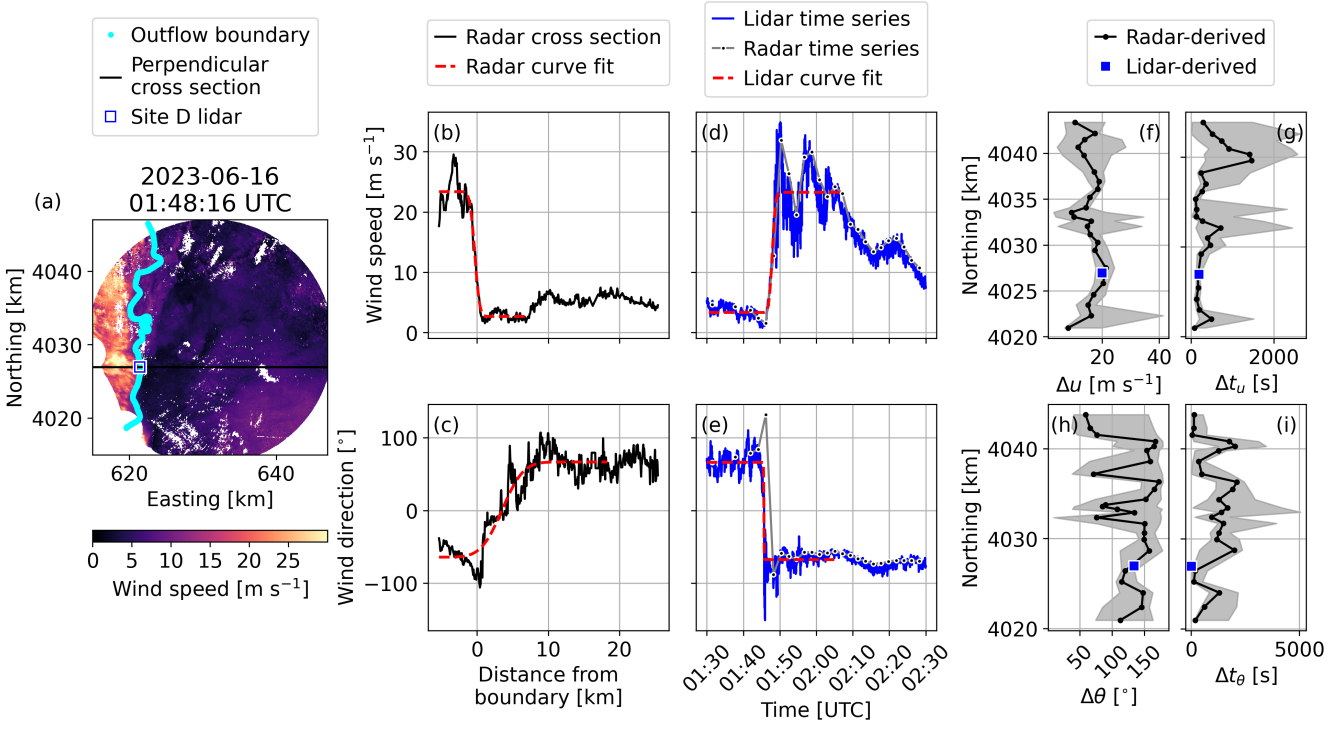

Figure 8. Comparison between the spatially and temporally defined ramp parameters using radar and lidar data, respectively, for the 2023-06-16 case. (a) Radar wind speed field at the time when the outflow boundary passes Site D. Cross section of radar-measured (b) wind speed and (c) direction along the line perpendicular to the outflow boundary at Site D, with the ramp function fit superimposed. Time series of lidar- and radar-measured (d) wind speed and (e) direction at Site D, with the ramp function fit superimposed. Comparison of ramp properties, including (f) wind speed amplitude, (g) wind speed rise time, (h) wind direction amplitude, and (i) wind direction rise time, from the spatially varying radar data and the temporally varying lidar data. The radar-derived parameters are presented as a median and interquartile range for each ~ 1 km section of the outflow boundary.

https://doi.org/10.5194/wes-2026-82
Preprint. Discussion started: 8 May 2026

Three of the four lidar-derived parameters match well with the radar-derived values, falling near the median and within the interquartile range at the corresponding location. The largest disagreement between the two methods is observed for Δt_θ, where the lidar-derived value is just below the range of radar-derived values. Panel (e) confirms that the wind direction changes over a short time, while panel (c) shows the change occurring over a relatively long distance. Figure 9 provides additional insight into this apparent discrepancy. Figure 9(a) and (b) show the wind direction field as the outflow boundary passes Site D. In panel (a), the wind direction east of Site D is $\sim 80°$ while the wind direction to the west is $\sim 290°$ (or $-70°$ as in Fig. 8). In panel (b), however, when the boundary is directly above Site D, a plume of $\sim 350°$ ($-10°$) wind direction flow appears east of the site. The radar-based ramp characterization method captures this plume (the black line perpendicular to the boundary intersects it in Fig. 9(b)), measuring a more gradual wind direction change, while the lidar-based method avoids the plume and detects a sudden wind direction change.

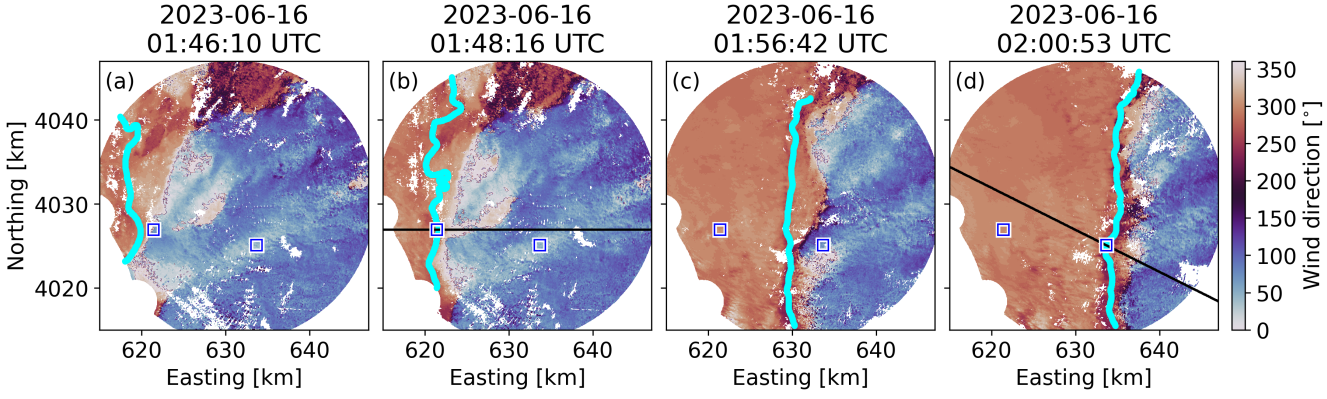

Figure 9. Radar-measured wind direction fields during the 2023-06-16 event at (a) 01:46:10 UTC, (b) 01:48:16 UTC, (c) 01:56:42 UTC, and (d) 02:00:53 UTC, with the outflow boundary (defined by the wind speed) superimposed in cyan. Squares mark the lidar locations at Sites D (west) and C1a (east). The black lines in panels (b) and (d) indicate the line perpendicular to the boundary at the lidar locations, where the wind speed and direction cross sections used for the ramp radar-based ramp function fit are extracted.

Figure 10 presents the same comparison at 02:00:53 UTC, when the outflow boundary has propagated through the radar domain to Site C1a. Once again, the temporally defined ramp parameters from the lidar generally agree well with the spatially defined values from the radar. In this case, the one exception is $\Delta\theta$, with the lidar-derived value 39° below the median radar-derived value. The wind direction fields in Fig. 9 show that Site C1a lies within a band of $\sim 50°$ wind direction before the boundary passes, while the surrounding flow is at $\sim 90°$. In Fig. 9(d), the line perpendicular to the boundary intersects the $90°$ wind direction region, measuring a change of $172°$ across the boundary (the wind direction is $\sim 280°$ or $-80°$ upstream of the boundary), while the lidar at C1a only detects a change of $110°$. These comparisons show that, while the spatial and temporal definitions of the wind ramp agree in general, flow features that vary in both space and time add complexity to the analysis. Both methods accurately characterize the wind ramp, but they capture slightly different features within the flow.

https://doi.org/10.5194/wes-2026-82
Preprint. Discussion started: 8 May 2026

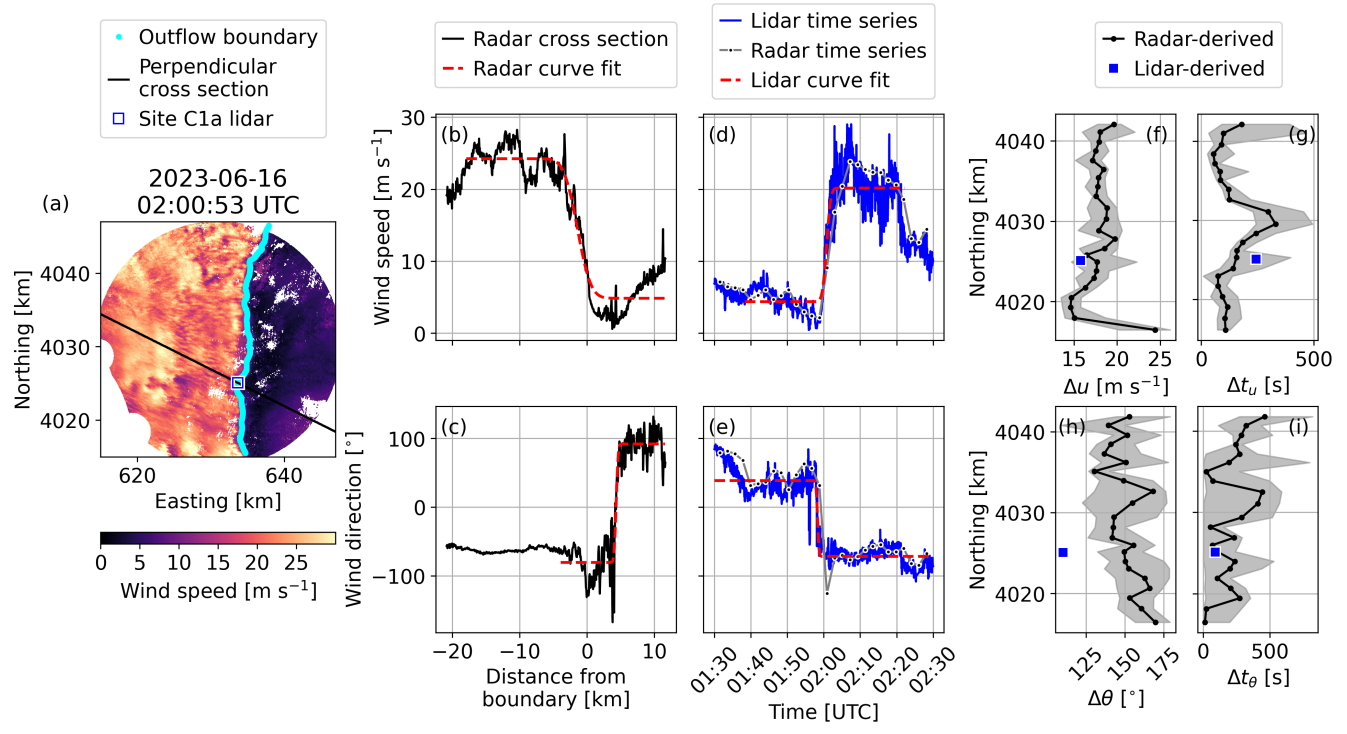

Figure 10. Comparison between the spatially and temporally defined ramp parameters using radar and lidar data, respectively, for the 2023-06-16 case. (a) Radar wind speed field at the time when the outflow boundary passes Site C1a. Cross section of radar-measured (b) wind speed and (c) direction along the line perpendicular to the outflow boundary at Site D, with the ramp function fit superimposed. Time series of lidar- and radar-measured (d) wind speed and (e) direction at Site C1a, with the ramp function fit superimposed. Comparison of ramp properties, including (f) wind speed amplitude, (g) wind speed rise time, (h) wind direction amplitude, and (i) wind direction rise time, from the spatially varying radar data and the temporally varying lidar data. The radar-derived parameters are presented as a median and interquartile range for each ∼ 1 km section of the outflow boundary.

7 Results and discussion

Having developed a method for characterizing thunderstorm outflow-induced wind ramps, we now discuss the results of this characterization and its implications. In particular, we focus on how well the IEC standard for the ECD represents the events observed here and why these findings are important for wind energy applications.

7.1 Comparison with IEC standard

We first compare the parameters obtained from our analysis with those prescribed in the IEC standard. To compare most directly, we linearly interpolate the parameters from the second and third radar heights (400 and 425 m MSL) to the mean hub height of the turbines in the King Plains wind farm, 418 m MSL, presented in Table 2. For the six cases studied here, the wind

https://doi.org/10.5194/wes-2026-82
Preprint. Discussion started: 8 May 2026

eawe european academy of wind energy
Open Access WIND ENERGY SCIENCE DISCUSSIONS

speed change is of a similar magnitude to that presented in the IEC standard (15 m s^{-1}), although some of the cases exhibit much lower values (e.g., 2023-07-01, where $\Delta u = 3.9$ m s^{-1}). Note that all cases exhibit the expected relationship between the maximum wind speed and the propagation speed, with $u_{\max}/V$ falling between 1.1 and 1.7, based on previous studies of thunderstorm outflows (e.g., Mahoney III (1988) observed $1.1 < u_{\max}/V < 2.3$). In all cases, Δt_u is substantially higher than the 10 s rise time described in the standard. The observed wind direction change is usually (but not always, e.g., 2023-06-16 and 2023-07-01) larger than that presented in the standard for the given hub-height wind speed. The wind direction rise times are once again much longer than the $\Delta t = 10$ s from the standard and even longer than the wind speed rise times in every case, consistent with the example shown in Fig. 7.

Table 2. The six thunderstorm outflow events analyzed in this study, including the parameter used to define the outflow boundary (wind speed or direction, as described in Section 5), the median parameters extracted from the radar data, interpolated to the mean King Plains turbine hub height, and the wind direction change prescribed by the IEC ($\Delta\theta_{\text{IEC}}$) for the given $u_{0,\text{hub}}$ value. Observed wind direction changes ($\Delta\theta$) are in the clockwise direction unless otherwise specified to be counterclockwise by "CCW".

Case	Boundary definition	$u_{0,\text{hub}}$ [m s^{-1}]	$\theta_{0,\text{hub}}$ [°]	Δu [m s^{-1}]	Δt_u [s]	$\Delta\theta_{\text{IEC}}$ [°]	$\Delta\theta$ [°]	Δt_θ [s]
2023-06-10	Direction	7.6	163.2	13.2	299.3	94.7	143.9	326.6
2023-06-16	Speed	4.1	75.8	17.2	155.8	175.6	146.4 (CCW)	159.2
2023-06-18	Direction	8.5	133.2	13.6	80.6	84.7	163.5	136.9
2023-07-01	Direction	9.9	186.3	3.9	76.5	72.7	52.1	513.5
2024-05-24	Direction	13.3	188.8	6.8	32.8	54.1	128.0	200.8
2024-07-03	Direction	11.8	170.4	5.4	151.9	61.0	157.9	310.5

We can also explore the variations of these parameters over time and height. In Fig. 11, we plot the median of all four parameters at four different heights for the 2023-06-16 and 2024-05-24 cases. In the 2023-06-16 case, Δu increases with height, while in the 2024-05-24 case, Δu decreases with height in the first part of the event, then switches to increasing with height around 10:05 UTC. As indicated by the values in Table 2, Δt_u is much larger in the 2023-06-16 case than in the 2024-05-24 case. The 2023-06-16 case also exhibits more variability in Δt_u over the duration of the event, especially at the 525 m MSL height. The two cases show opposite trends with height for $\Delta\theta$, with the 2023-06-16 case increasing with height and the 2024-05-24 case decreasing. In the 2023-06-16 case, Δt_θ starts at an unusually large value, then decreases nearly an order of magnitude by 01:55 UTC. For the remainder of the event, Δt_θ exhibits an increasing trend with height. In the 2024-05-24 case, however, Δt_θ is nearly invariant with height and time. For all parameters, variability with time can be attributed to interactions with undulations in terrain or with the wind farms themselves as the outflow boundary passes through the radar domain. Wind farms have been shown to influence large-scale atmospheric boundary layer processes in general (Abraham et al., 2025), and specifically the behavior of thunderstorm outflows (Tomaszewski and Lundquist, 2021). The results discussed above demonstrate that each event behaves differently, likely capturing thunderstorm outflows at different stages of their life cycle, which affects the depth, speed, and shape of the outflow (Wakimoto, 1982). Thunderstorm type or formation mechanism has also been shown to influence the properties of the outflow-induced wind ramp (Lombardo et al., 2014).

https://doi.org/10.5194/wes-2026-82
Preprint. Discussion started: 8 May 2026

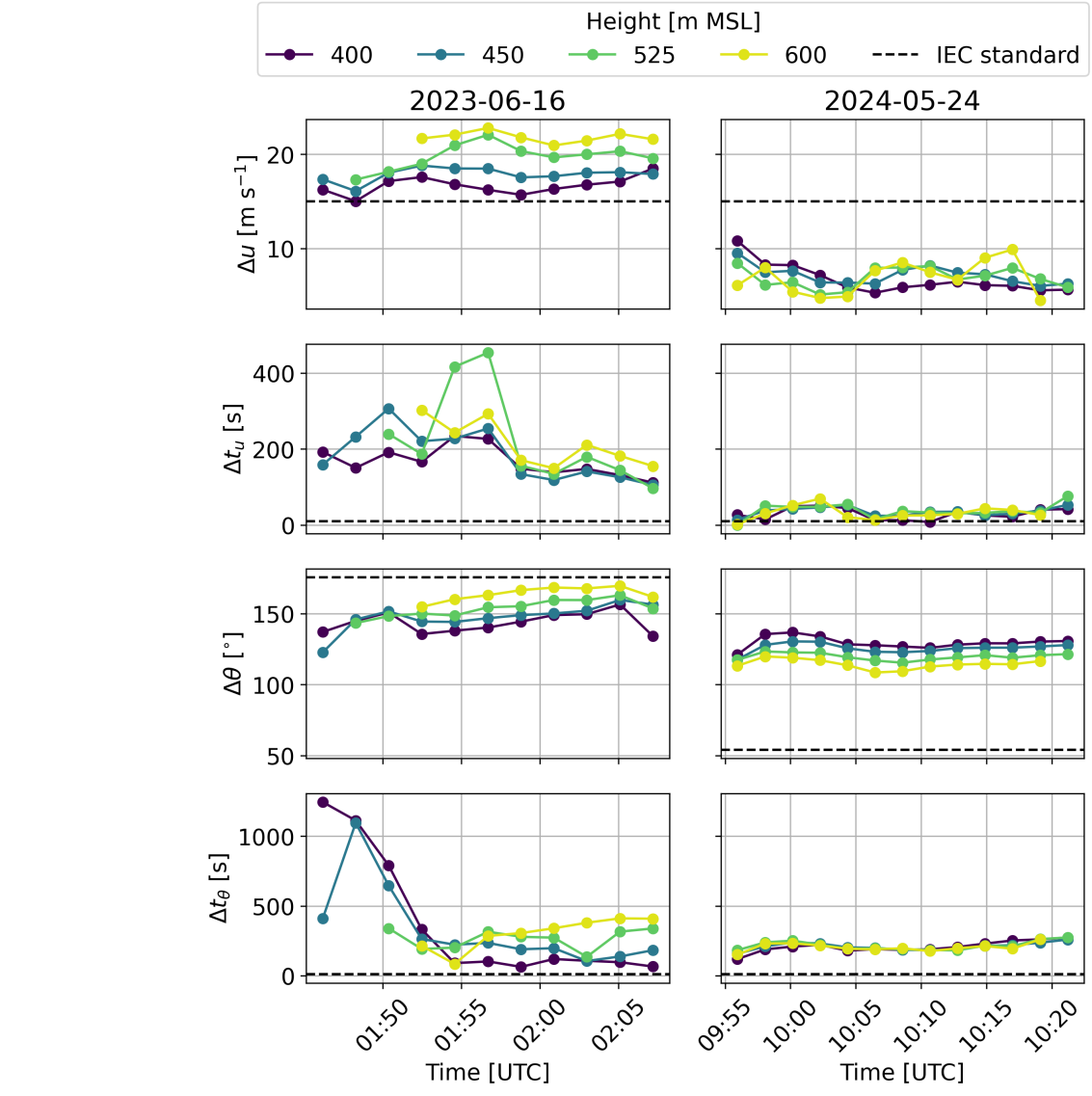

Figure 11. Evolution of wind ramp parameters over the duration of the outflow boundary within the radar domain for two of the six cases. Four heights are shown, with each point representing the median value of the parameter at that point in time and height.

Based on the cases investigated here, we can highlight several deviations from the IEC standard ECD case. First, the wind speed and direction cross sections and time series do not follow the idealized ramp shape. Other features are often observed, such as a decrease in wind speed just before the ramp, and oscillations in wind speed just after (see e.g., Figs. 8 and 10). Not only do these features complicate the process of wind ramp characterization, they also impact the turbines encountering these events. The decrease in wind speed just before the ramp effectively increases the magnitude to the wind speed change

https://doi.org/10.5194/wes-2026-82
Preprint. Discussion started: 8 May 2026

eawe european academy of wind energy
Open Access WIND ENERGY SCIENCE DISCUSSIONS

experienced by the turbine, while the high wind speed oscillations can increase fatigue loads and complicate the turbine control strategy (see Sect. 7.2). These features are not captured in the IEC ECD definition.

Additionally, we observe significant variability between events. No single description of an ECD can be applied to all events, even considering that we only show examples of wind ramps generated by thunderstorm outflows and do not attempt to generalize to all wind ramps. However, the ECD is intended to represent a worst-case scenario that the turbine must withstand rather than a general description of all wind ramps that the turbine will experience. Some of the cases observed here exhibit parameters that exceed this worst-case scenario. For example, the 2023-06-16 case exhibits a wind speed rise of 17.2 m s^{-1}, even larger than the 15 m s^{-1} in the standard. Four of the six cases exhibit wind direction changes larger than those described in the standard. These observed events are not necessarily more extreme for a wind turbine, however, because the timescales are so much longer. A change in wind speed and direction over the 10 s prescribed in the standard could be more damaging to a turbine than the longer timescale changes observed here, even if the magnitudes are smaller, because the turbine has less time to react by adjusting control parameters such as yaw, pitch, and generator torque. Furthermore, observed wind speed and direction changes are not synchronized. In Sect. 5 we show that they do not change at the same time, and here we show that they do not change at the same rate, either (i.e., $\Delta t_u \neq \Delta t_\theta$). This lag between the wind direction and speed change may further lessen the stress on the turbines because they can start yawing into the wind before having to adjust to a sudden increase in wind speed. With this lag, the turbine is not slammed with a gust while the rotor is severely misaligned with the wind. For the reasons described above, wind ramps induced by thunderstorm outflows are not expected to generate significantly stronger loading than that for which the turbine is designed, assuming it is designed to withstand the ECD case described by the IEC standard. Instead, these large-scale thunderstorm outflow events are expected to have more important implications for overall wind farm power generation than individual turbine loads, as explained in more detail in Sect. 7.2.

7.2 Implications of spatial variability for wind energy applications

As seen in Figs. 8 and 10, ramp properties vary significantly along the outflow boundary. These variations are attributed to a combination of interactions with terrain and wind farms, as discussed in the previous section, and spatial heterogeneity of the outflow itself (Mahoney III, 1988). To understand how this spatial variability affects the wind turbines and their power generation, we examine the wind speed ramp properties near the three instrumented turbines marked in Fig. 2. Figure 12(a) shows the radar wind speed field when the boundary is closest to all three turbines (02:07:12 UTC), at the 400 m MSL height, which is the closest radar level to the hub height of these turbines. At this height, radar data are unavailable in the northeast corner of the domain due to variations in terrain and the curvature of the earth. Comparisons of the wind speed amplitude and rise time across the boundary, derived from the spatially varying radar data and the temporally varying turbine anemometer data, are presented in Fig. 12(b) and (c), respectively. At its northernmost edge, the boundary is very close to the eastern edge of the radar domain, causing the increased uncertainty in Δu and Δt_u seen in the plots. The time series used to characterize the wind speed ramp for the turbines are presented in panels (d), (e), and (f), along with the time series of radar-measured wind speed at the nearest radar grid points. Some discrepancies are observed between the radar- and turbine-measured wind speeds. Because the radar beams are 0.5° wide, they cover a larger volume farther from the radars, causing a smoothing effect that is

https://doi.org/10.5194/wes-2026-82
Preprint. Discussion started: 8 May 2026

eawe european academy of wind energy
Open Access WIND ENERGY SCIENCE DISCUSSIONS

more prominent at large distances, such as those presented in this figure. Furthermore, the turbine anemometers are located on the nacelle, behind the turbine rotor, where complex local flows influence their measurements (St. Martin et al., 2017). These considerations contribute to the differences in the values of Δu and Δt_u derived from the different instruments, along with the ~ 1 km eastward offset of the turbines from the outflow boundary at the presented time.

Both the radars and the turbine anemometers show that Δu can vary more than 5 m s^{-1} within a few kilometers along the boundary (Fig. 12(b)), while Δt_u changes ~ 200 s within the same distance (Fig. 12(c)). The lower panels of the figure demonstrate the impact of this variability on turbine power generation. All three turbines experience low wind speeds, around the turbine cut-in speed, before the passage of the outflow boundary. When the wind speed rises around 02:07 UTC, turbines F04 and G02 immediately increase their power generation, reaching rated power ($P/P_{\text{rated}} = 1$) by 02:10 UTC. Turbine E06, however, remains at $P/P_{\text{rated}} = 0$ until 02:30 UTC. This behavior is attributed to the properties of the wind ramp experienced by this turbine. The wind speed changes substantially ($\Delta u = 19.5$ m s^{-1}) in just over a minute ($\Delta t_u = 69.5$ s). Furthermore, Fig. 12(d) shows that the wind speed overshoots the cut-out wind speed by 14 m s^{-1} and remains above cut-out for a few minutes. It decreases for the next few minutes, before increasing again to the same 39 m s^{-1} value. The turbine only begins producing power once the wind speed has remained below cut-off for several minutes, 20 minutes after the other two turbines. This hysteresis around the cut-out wind speed is a common way to prevent turbines from cutting in and out repeatedly at maximum power when the wind is oscillating around the cut-out speed.

These results show that it is difficult to predict turbine response to a thunderstorm outflow event. The three turbines presented here are located in neighboring wind farm rows, but they produce very different amounts of power while experiencing the same event. This variability introduces challenges for predicting the overall wind farm power. When such local variations in wind speed cause one turbine to produce no power while its neighbor produces full rated power, the wind farm power can then range anywhere from 0 to $N \times P_{\text{rated}}$, where N is the number of turbines in the farm. These thunderstorm outflow events substantially increase uncertainty for wind farm and grid operators during extreme weather events when grid reliability is crucial.

8 Conclusions

The current study characterizes the spatially and temporally evolving behavior of six wind ramps generated by thunderstorm outflow events using dual-Doppler X-band radar data collected during the AWAKEN campaign. Outflow boundaries are automatically detected and tracked through the radar domain, then wind ramp properties are obtained using a curve-fitting algorithm. These properties are compared to those described in the IEC standard for an “extreme coherent gust with direction change (ECD)”. The observed events exhibit wind speed and direction changes of similar magnitudes to those in the standard but over timescales an order of magnitude larger. The observations also show complexities that are not captured by the standard, including variations with height and time as well as deviations from the simple ramp profile. Furthermore, strong spatial variability along the outflow boundary is observed, posing challenges for wind farm power forecasting during extreme weather events.

https://doi.org/10.5194/wes-2026-82
Preprint. Discussion started: 8 May 2026

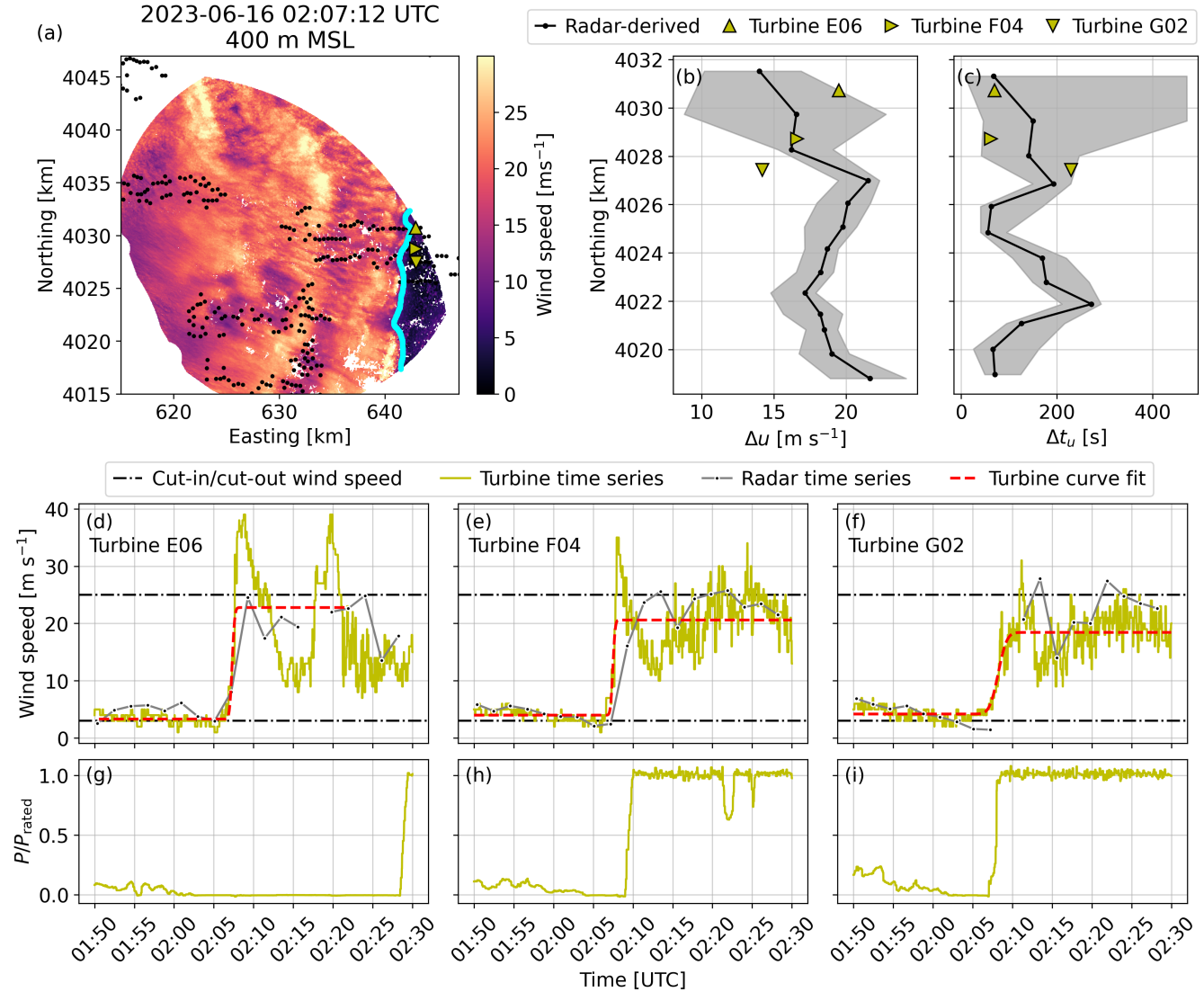

Figure 12. (a) Radar wind speed field at 400 m MSL at the time when the outflow boundary passes nearest to the three instrumented turbines. The cyan line indicates the outflow boundary, black points mark the locations of all wind turbines within the domain, and the gold triangles indicate the three instrumented turbines, as shown in Fig. 2. Ramp properties, including (b) wind speed amplitude and (c) wind speed rise time, derived from the spatially varying radar data and the temporally varying turbine anemometer data. Time series of turbine- and radar-measured wind speeds for turbines (d) E06, (e) F04, and (f) G02, with the ramp function fit to the turbine anemometer data superimposed. Cut-in and cut-out wind speeds are indicated by the dot-dashed black lines. Time series of normalized power generated by turbines (g) E06, (h) F04, and (i) G02.

https://doi.org/10.5194/wes-2026-82
Preprint. Discussion started: 8 May 2026

eawe european academy of wind energy
Open Access WIND ENERGY SCIENCE DISCUSSIONS

The results of this study can be used to address these challenges. First, weather forecasting models can use these data to validate and refine their predictions. If thunderstorm outflows can be modeled in more detail, more accurate power forecasts are possible. In addition, the findings of the current investigation can inform the design of advanced wind farm control strategies that maximize power generation and minimize structural damage from extreme wind ramps. For example, consensus control, the use of wind direction information from multiple turbines to improve collective alignment with the wind (Annoni et al., 2019), could be adapted to help downstream turbines anticipate the large wind direction changes observed during thunderstorm outflow events. Alternatively, instruments could be configured to measure upstream of the entire wind farm to collect data about incoming changes in wind conditions. A wind farm controller could then prepare the turbines for the wind they will soon encounter.

To determine whether investing in the development of such technologies is worthwhile, we must first understand the frequency and severity of thunderstorm outflow events worldwide and their financial costs in terms of power loss and structural damage to turbines. Other types of extreme weather events, such as hurricanes and tornadoes, should also be investigated. Future work can then investigate the application of the advanced modeling and control techniques discussed above to multiple types of extreme events that wind farms experience. Extreme weather events are expected to impact other energy infrastructure, such as transmission and distribution lines, contributing to power outages. Future work will explore the impacts of these events on the reliability and resilience of the electricity grid.

Data availability. Radar and met station datasets are publicly available on the Wind Data Hub: https://doi.org/10.21947/1959708 (Goldberger, 2024), https://doi.org/10.21947/1958709 (Hirth and Zalkind, 2025a), https://doi.org/10.21947/1958710 (Hirth and Zalkind, 2025b), https://doi.org/10.21947/1958708 (Hirth and Zalkind, 2025c).

Author contributions. AA conducted the conceptualization, methodology development, and formal analysis. NB and NH supervised the work. BH and JS were responsible for radar data collection and curation. PM led the AWAKEN project. AA wrote the original draft, which all authors reviewed and edited.

Competing interests. The contact author has declared that none of the authors has any competing interests.

Disclaimer. The views expressed in the article do not necessarily represent the views of the DOE or the U.S. Government.

Acknowledgements. This work was authored in part by the National Laboratory of the Rockies for the U.S. Department of Energy (DOE), operated under Contract No. DE-AC36-08GO28308. Funding was provided by the U.S. Department of Energy Office of Critical Minerals

https://doi.org/10.5194/wes-2026-82
Preprint. Discussion started: 8 May 2026

and Energy Innovation Wind Energy Technologies Office. The provision of the profiling lidar at site D was financed by the German Federal Ministry for Economic Affairs and Climate Action (BMWK) as part of the project Windpark Radar (funding code 03EE3031A). The authors thank Julie Lundquist and Lin-Ya (Lilian) Hung for providing high-resolution lidar data. The authors would also like to thank the Wind Data Hub team for making the AWAKEN field campaign data publicly available.

https://doi.org/10.5194/wes-2026-82
Preprint. Discussion started: 8 May 2026

eawe european academy of wind energy
Open Access WIND ENERGY SCIENCE DISCUSSIONS

References

Abraham, A., Puccioni, M., Jordan, A., Maric, E., Bodini, N., Hamilton, N., Letizia, S., Klein, P. M., Smith, E. N., Wharton, S., et al.: Operational wind plants increase planetary boundary layer height: an observational study, Wind Energy Science, 10, 1681–1705, https://doi.org/https://doi.org/10.5194/wes-10-1681-2025, 2025.

Annoni, J., Bay, C., Johnson, K., Dall'Anese, E., Quon, E., Kemper, T., and Fleming, P.: Wind direction estimation using SCADA data with consensus-based optimization, Wind Energy Science, 4, 355–368, https://doi.org/https://doi.org/10.5194/wes-4-355-2019, 2019.

Arthur, R. S., Mirocha, J. D., Marjanovic, N., Hirth, B. D., Schroeder, J. L., Wharton, S., and Chow, F. K.: Multi-scale simulation of wind farm performance during a frontal passage, Atmosphere, 11, 245, https://doi.org/https://doi.org/10.3390/atmos11030245, 2020.

Canepa, F., Burlando, M., and Solari, G.: Vertical profile characteristics of thunderstorm outflows, Journal of Wind Engineering and Industrial Aerodynamics, 206, 104 332, https://doi.org/https://doi.org/10.1016/j.jweia.2020.104332, 2020.

Canny, J.: A computational approach to edge detection, IEEE Transactions on pattern analysis and machine intelligence, PAMI-8, 679–698, https://doi.org/10.1109/TPAMI.1986.4767851, 1986.

Droegemeier, K. K. and Wilhelmson, R. B.: Numerical simulation of thunderstorm outflow dynamics. Part I: Outflow sensitivity experiments and turbulence dynamics, Journal of atmospheric sciences, 44, 1180–1210, https://doi.org/https://doi.org/10.1175/1520-0469(1987)044<1180:NSOTOD>2.0.CO;2, 1987.

Goldberger, L.: Site C1 PNNL Surface Met Station / Reviewed Data, https://doi.org/10.21947/1959708, 2024.

Gunter, W. S. and Schroeder, J. L.: High-resolution full-scale measurements of thunderstorm outflow winds, Journal of Wind Engineering and Industrial Aerodynamics, 138, 13–26, https://doi.org/https://doi.org/10.1016/j.jweia.2014.12.005, 2015.

Hannesdóttir, Á. and Kelly, M.: Detection and characterization of extreme wind speed ramps, Wind Energy Science, 4, 385–396, https://doi.org/https://doi.org/10.5194/wes-4-385-2019, 2019.

Hirth, B. and Zalkind, D.: TTU-X1 Raw Data, https://doi.org/10.21947/1958709, 2025a.

Hirth, B. and Zalkind, D.: TTU-X2 Raw Data, https://doi.org/10.21947/1958710, 2025b.

Hirth, B. and Zalkind, D.: TTU-X Dual Doppler Synthesis, https://doi.org/10.21947/1958708, 2025c.

Hirth, B., Schroeder, J., and Guynes, J.: An Onshore Deployment of Advanced Dual-Doppler Radar for Wind Energy Applications, in: Journal of Physics: Conference Series, vol. 2745, p. 012013, IOP Publishing, https://doi.org/10.1088/1742-6596/2745/1/012013, 2024.

Hirth, B. D., Schroeder, J. L., Irons, Z., and Walter, K.: Dual-Doppler measurements of a wind ramp event at an Oklahoma wind plant, Wind Energy, 19, 953–962, https://doi.org/https://doi.org/10.1002/we.1867, 2016.

IEC: Wind energy generation systems – Part 1: Design requirements, Standard IEC 61400-1:2019, International Electrotechnical Commission, Geneva, Switzerland, 2019.

Kelly, M., Andersen, S. J., and Hannesdóttir, Á.: Statistical impact of wind-speed ramp events on turbines, via observations and coupled fluid-dynamic and aeroelastic simulations, Wind Energy Science, 6, 1227–1245, https://doi.org/https://doi.org/10.5194/wes-6-1227-2021, 2021.

Lombardo, F. T., Smith, D. A., Schroeder, J. L., and Mehta, K. C.: Thunderstorm characteristics of importance to wind engineering, Journal of Wind Engineering and Industrial Aerodynamics, 125, 121–132, https://doi.org/https://doi.org/10.1016/j.jweia.2013.12.004, 2014.

Mahoney III, W. P.: Gust front characteristics and the kinematics associated with interacting thunderstorm outflows, Monthly weather review, 116, 1474–1492, https://doi.org/https://doi.org/10.1175/1520-0493(1988)116<1474:GFCATK>2.0.CO;2, 1988.

https://doi.org/10.5194/wes-2026-82
Preprint. Discussion started: 8 May 2026

Moriarty, P., Bodini, N., Letizia, S., Abraham, A., Ashley, T., Bärfuss, K. B., Barthelmie, R. J., Brewer, A., Brugger, P., Feuerle, T., et al.: Overview of preparation for the American WAKE ExperimeNt (AWAKEN), Journal of Renewable and Sustainable Energy, 16, https://doi.org/https://doi.org/10.1063/5.0141683, 2024.

Pichugina, Y. L., Banta, R. M., Strobach, E., Carroll, B., Brewer, W. A., Turner, D., Wulfmeyer, V., James, E., Lee, T., Baidar, S., et al.: Case study of a bore wind-ramp event from lidar measurements and HRRR simulations over ARM Southern Great Plains, Journal of Renewable and Sustainable Energy, 16, https://doi.org/https://doi.org/10.1063/5.0161905, 2024.

St. Martin, C. M., Lundquist, J. K., Clifton, A., Poulos, G. S., and Schreck, S. J.: Atmospheric turbulence affects wind turbine nacelle transfer functions, Wind Energy Science, 2, 295–306, https://doi.org/https://doi.org/10.5194/wes-2-295-2017, 2017.

Storm Prediction Center (SPC), NOAA: SPC Maps, Graphics, and Data (WCM Page), https://www.spc.noaa.gov/wcm/, last updated 13 May 2025; accessed: 2025-12-01, 2025.

Tomaszewski, J. M. and Lundquist, J. K.: Observations and simulations of a wind farm modifying a thunderstorm outflow boundary, Wind Energy Science, 6, 1–13, https://doi.org/https://doi.org/10.5194/wes-6-1-2021, 2021.

U.S. Department of Energy: U.S. Installed and Potential Wind Power Capacity and Generation, https://windexchange.energy.gov/maps-data/321, accessed: 2025-12-01, 2025.

Valldecabres, L., von Bremen, L., and Kühn, M.: Minute-scale detection and probabilistic prediction of offshore wind turbine power ramps using dual-Doppler radar, Wind Energy, 23, 2202–2224, https://doi.org/https://doi.org/10.1002/we.2553, 2020.

van der Walt, S., Schönberger, J. L., Nunez-Iglesias, J., Boulogne, F., Warner, J. D., Yager, N., Gouillart, E., and Yu, T.: scikit-image: image processing in Python, PeerJ, 2, e453, https://doi.org/10.7717/peerj.453, 2014.

Wakimoto, R. M.: The life cycle of thunderstorm gust fronts as viewed with Doppler radar and rawinsonde data, Monthly weather review, 110, 1060–1082, https://doi.org/https://doi.org/10.1175/1520-0493(1982)110<1060:TLCOTG>2.0.CO;2, 1982.

Wallace, J. and Hobbs, P.: Atmospheric Science: An Introductory Survey, Elsevier, Burlington, 2nd edn., ISBN 0-12-732951-X, 2006.